A radiation belt of energetic protons located between Saturn and its rings

E. Roussos, P. Kollmann, N. Krupp, A. Kotova, L. Regoli, C. Paranicas, D. G Mitchell, S. M Krimigis, D. Hamilton, P. Brandt, et al.

Energetic protons trapped between Saturn and its rings

E. Roussos,[1*] P. Kollmann,[2] N. Krupp,[1] A. Kotova,[3] L. Regoli,[4] C. Paranicas,[2]
D. G. Mitchell,[2] S. M. Krimigis,[2,5] D. Hamilton,[6] P. Brandt[2], J. Carbary,[2]
S. Christon, [7] K. Dialynas,[5] I. Dandouras,[3] M. E. Hill,[2] W. H. Ip, [8] G. H. Jones,[9,10]
S. Livi,[11] B. H. Mauk,[2] B. Palmaerts,[12] E. C. Roelof,[2] A. Rymer,[2]
N. Sergis,[5,13] H. T. Smith[2]

[1]Max Planck Institute for Solar System Research, 37077, Goettingen, Germany
[2]Johns Hopkins University Applied Physics Laboratory, Laurel, MD 20723-6099, USA
[3]IRAP, Université de Toulouse, CNRS, UPS, CNES, Toulouse, France
[4]Department of Climate and Space Sciences and Engineering,
University of Michigan, 48109-2143 Ann Arbor, USA
[5]Office of Space Research and Technology Academy of Athens, 11527, Greece
[6]University of Maryland, College Park, MD 20742, USA
[7]Focused Analysis and Research, MD 11043, USA
[8]Institute of astronomy, National Central University, 32001 Jhongli, Taiwan
[9]UCL Mullard Space Science Laboratory, Dorking, Surrey RH5 6NT ,UK
[10]The Centre for Planetary Sciences at UCL/Birkbeck, London WC1E 6BT, UK
[11]Southwest Research Institute, USA
[12]University of Liege, Belgium
[13]National Observatory of Athens, 15236 Penteli, Greece

[*]To whom correspondence should be addressed; E-mail: roussos@mps.mpg.de
E. Roussos and P. Kollmann contributed equally to this manuscript.

Cassini's Magnetosphere Imaging Instrument has obtained the first measurements of a radiation belt that resides just above Saturn's dense atmosphere and is permanently decoupled from the rest of the magnetosphere through a 62000-km wide particle absorbing corridor formed by the planet's A to C-

rings. This belt extends across Saturn's D-ring and comprises mostly $\sim$0.025 - $>$1 GeV protons produced through Cosmic Ray Albedo Neutron Decay (CRAND). CRAND is balanced by proton losses to atmospheric neutrals and D-ring dust rather than by magnetospheric diffusion which affects the belts beyond the rings. Strong proton depletions mapping onto the D-ring's D68 and D73 ringlets contrast with the absence of notable proton losses along its D72 ringlet, and reveal a highly-structured and diverse dust environment configuration near Saturn.

Introduction

During the Proximal Orbit phase of the Cassini mission (23 April - 15 September 2017), the spacecraft completed 22 crossings through the narrow gap between Saturn's upper atmosphere and its rings (Figure 1) and performed the first in-situ measurements of the local energetic charged particle environment with the Magnetosphere Imaging Instrument, MIMI (*1*).

Observational evidence that trapped particle radiation may be confined inward of Saturn's rings was first obtained during Cassini's Saturn Orbit Insertion (SOI, 1 July 2004) through Energetic Neutral Atom (ENA) imaging of this region by MIMI (*2*). These observations revealed an emission of 20 to 50 keV/nucleon ENAs coming from a low-altitude, trapped ion population of the same energy, which was subject to charge-exchange with neutral atoms of Saturn's upper atmosphere. The ions that produced the low altitude ENA emission are thought to derive from planetward ENAs generated in Saturn's middle magnetosphere (*3, 4*). Following their re-ionization through charge-stripping reactions in the planet's upper atmosphere, the newly converted ions get temporarily trapped by the planet's magnetic field, before charge exchange converts them back into the ENAs that MIMI detected (*2*). The exact altitude of the ion population driving this ENA emission is unknown but could be similar to that of the 0.06-1 MeV

ions that were recently detected between 4300 and 18000 km above Jupiter's 1-bar atmospheric level and were possibly generated by the same mechanism (multiple charge-exchange) (*5*).

Higher energy protons, at MeV energies and above, can be supplied to the inner trapping region through the Cosmic Ray Albedo Neutron Decay process (CRAND), as it was initially pointed out by (*6*) and (*7*). CRAND protons are among the β-decay products of secondary (albedo) neutrons which form after Galactic Cosmic Rays (GCRs) impact Saturn's atmosphere and/or its dense rings. Because neutrons are not bound by the planetary magnetic field, they can fly away from their generation site and through the trapping region, within which they may release their β-decay proton. CRAND is a key process sustaining the proton radiation belts of Earth and those of Saturn outside its rings ("main radiation belts") (*8–12*).

While CRAND undoubtedly generates energetic protons near the planet, it was not clear before Cassini's Proximal orbits whether these protons could accumulate in large numbers and form a localized radiation belt. Quantitative models that were used to predict upper limits of the proton intensities in this region (*13*) relied on a series of input parameter extrapolations and simplifying assumptions for the determination of the CRAND source rate and the loss rates of protons to atmospheric neutrals and to ring dust. In particular, it was not known if there would be a significant signal from energetic protons across the D-ring ($\sim$1.11 - 1.24 $\mathrm{R_S}$) (*14*) and its three ringlets, named as D68, D72 and D73 and centered at 1.12, 1.19 and 1.22 $\mathrm{R_S}$, respectively (*15, 16*), all of which are contained within the trapping region. The input values for the description of the D-ring properties were so poorly constrained that even the most realistic predictions for the 10-60 MeV proton fluxes spread over two orders of magnitude, with the lowest values near MIMI's detection limits.

The simulations indicated that the dynamics of MeV protons in this inner radiation belt would be determined by physical processes different from those affecting protons of the main radiation belts. Proton intensities in Saturn's main radiation belts are limited by radial diffusion,

which controls how fast these particles are distributed within the orbits of the planet's large icy moons, where they get subsequently absorbed (*12,17*). Similarly, radial diffusion near the planet could act as a proton sink by gradually moving protons to the massive C-ring (1.24 - 1.53 $\mathrm{R_S}$) and the dense atmosphere ($\lesssim$1.02 $\mathrm{R_S}$). Since, however, radial diffusion rates near the planet were projected to be extremely low (*17, 18*), it was instead proposed that the intensity of the proton fluxes would be primarily determined by a balance of the CRAND source rate against losses of protons to dust and neutral gas. Losses to the equatorially confined dust, in particular, can be transmitted along the magnetic field lines sampled by Cassini's high-inclination Proximal orbit trajectory, allowing MIMI to obtain radial dust density scans of the D-ring system from a large distance (e.g. Figure 1, red lines), a capability not available to other in-situ instruments of Cassini (e.g. (*19*)).

Probing the local dust and gas environment and the CRAND source is further simplified because proton populations of the inner trapping region are permanently isolated from the rest of the magnetosphere. Saturn's dense A to C-rings form a $\approx$ 62000-km wide particle absorbing corridor (1.24-2.27 $\mathrm{R_S}$) that is impermeable for any magnetospheric particle that gets transported inward of 2.27 $\mathrm{R_S}$. Mixing of energetic particle populations near the planet from different source locations (*10*), which may occur at Earth and Jupiter and complicate the interpretation of relevant measurements, is inhibited at Saturn. This filtering is also important for unambiguously detecting CRAND electrons, the other β-decay product of albedo neutrons, the presence of which was only recently resolved at the Earth (*20*). Furthermore, the strong magnetic field near Saturn forms a very stable energetic charged particle trapping environment that is unresponsive to solar wind or magnetospheric transients that affect the magnetosphere at larger distances. Finally, the location of the inner trapping region establishes a constant source rate for CRAND protons and electrons, since the primary GCR energies that drive CRAND and define its source strength, exceed 20 GeV (*21*). GCRs above this energy show no sign of

heliospheric modulation (*22*). The stability of the CRAND source rate, in particular, has proven useful to unambiguously decompose the contribution of different magnetospheric processes that control the evolution of Saturn's main radiation belts (*12*).

In the following sections we present MIMI's ground-truth measurements of trapped protons, ions and electrons in Saturn's innermost trapping region and we discuss the findings in the context of the theory, simulations and past observations discussed above.

Instrumentation and methodology

Magnetosphere Imaging Instrument (MIMI): The MIMI instrument (*1*) comprises three different sensors, the Low Energy Magnetospheric Measurement System (LEMMS), the Charge-Energy Mass Spectrometer (CHEMS), and the Ion Neutral Camera (INCA).

Here we rely mostly on LEMMS, which is a double-ended, charged particle telescope that based on the latest calibration (*23*) can measure the energy and angular distribution of 27 keV to >300 MeV protons and of 18 keV to ∼10 MeV electrons. Certain LEMMS channels can also distinguish heavier MeV ions from protons but lack mass resolution (*24*). CHEMS has three particle telescopes which measure the energy, mass, and charge state of energetic ions between 3 and 220 keV/e. INCA obtains Energetic Neutral Atom (ENA) images in oxygen and hydrogen, as well as high sensitivity ion spectra in the energy range from 7 keV/nucleon to 8 MeV/nucleon.

Methods: The majority of the results presented here are based on observations by LEMMS channels P8 (>25 MeV H^+) and E7 (>300 MeV H^+ and >7 MeV e^-). These two channels achieve the most efficient rejection of instrument penetrating protons that can contaminate the measurements. We occasionally cite channel P9 (>60 MeV H^+ and >1 MeV e^-), due to its high-sensitivity, omnidirectional proton response. Unless otherwise stated, we will quote chan-

nels P8, E7 and P9 by referring to their proton energy response, since the respective measurements are dominated by protons, as we later explain. Designations of other LEMMS electron or ion channels will be given when relevant observations are shown.

Differential proton flux spectra were obtained through a forward model that reconstructs the >25 MeV and >300 MeV count rates by convolving those channels angular and energy response functions with predefined shapes of proton energy spectra and angular distributions (*23*) (Figures S.2, S.5). For lower proton energies or non-proton species, LEMMS, CHEMS and INCA could only provide upper flux limits. The determination of the upper limits is also detailed in (*23*) (Figure S.7).

In order to magnetically map the in-situ measurements by MIMI, we calculated the L-shell, the equatorial pitch angle and the loss-cone through an empirical third-order magnetic field model (*25*). We define the L-shell (L) as Cassini's field line distance from Saturn's rotation axis along the magnetic equator, normalized to a planetary radius. The equatorial pitch angle (α_{eq}) is the angle between the proton velocity and the magnetic field at the magnetic equator, while the loss-cone corresponds to the pitch angle below which the mirror altitude of the trapped particles is lower than 1000 km, well into the dense atmosphere.

Innermost energetic particle trapping region observations

Raw proton data: The raw count rates of >25 MeV, >300 MeV and >60 MeV protons are plotted in Figure 2 as a function of L, from all the times that Cassini was magnetically connected to regions inwards of Saturn's C-ring. We can identify several major features in this L-shell profile even before we convert these raw count rates to physical units.

We find a strong signal on magnetic field lines that thread through the D-ring, even though trapped energetic protons at those L-shells bounce through that ring every few seconds and could sustain heavy losses. The effects of proton absorption from two of the D-ring's ringlets

are more severe. The count rate dropout that develops at the outer boundary of the trapping region maps to the location of the D73 ringlet (which extends over 0.02 $\mathrm{R_S}$) instead of the C-ring and makes the radiation belt slightly narrower than initially expected, since the presence of the ringlets was not taken into account in past simulations (*13*). A second major count rate dropout, which splits the inner radiation belt in two main segments, is seen at the L-shell of the D68 ringlet. No obvious absorption signature is observed in association with the D72 ringlet.

In agreement with model predictions (*13*), the dense upper atmosphere limits the intensities of trapped radiation towards the lowest L-shells. The high sensitivity, omnidirectional >60 MeV proton measurements (Figure 2C) registered counts at levels above the instrumental background down to L$\sim$1.03, indicating that some minimal flux of MeV protons may survive down to at least 1800 km above the 1-bar atmospheric pressure level.

Proton pitch angle distributions: The large scatter of the MeV proton rates observed at any given L-shell (Figure 2), can be attributed to changes in both the spacecraft's latitude and LEMMS's equatorial pitch angle pointing, α_{eq} (Figure S1, (*23*)). A successful reconstruction of these two dominant dependencies (Figure S.4 (*23*)), requires the actual proton pitch angle distribution (PAD) is much steeper than what is observed with the coarse angular resolution of LEMMS. If we describe the PAD as $\propto \sin^N \alpha_{eq}$ outside the loss cone, we obtain that the power, N, ranges between 10 (at the D-ring) and 100 (near the atmosphere). For reference, this exponent is lower than $\sim$6 in Saturn's main proton radiation belts (*26–28*).

Any residual signal not reproduced by the aforementioned reconstruction indicates that temporal variations, if present, may only account for changes comparable to or smaller than the 1σ statistical uncertainty in the LEMMS signal.

Proton energy spectra ($\geqslant$25 MeV): Differential proton intensities were evaluated assuming a spectral form that is a simple power law in energy and has a cutoff at 20 GeV. Even if Saturn's

magnetic field can stably trap even higher energies (*29*), the proton gyroradius above 20 GeV becomes comparable to the width of the trapping region (*30*). The resulting spectrum at L=1.1, where the proton intensities peak, is plotted in Figure 3A.

We find that the proton spectrum is hard (meaning that flux decreases slowly with increasing energy), with a spectral index of $\sim$-1. For such a spectrum, relativistic protons ($>$0.938 GeV) could make up a considerable contribution to the count rate of the $>$300 MeV channel. The fact that the $>$300 MeV proton channel recorded counts even when LEMMS was pointing well into the atmospheric loss cone (Figure 2A,B, S1.A), is an indirect but independent verification that relativistic protons contribute to the measurements: such counts may only come from $>$0.9 GeV instrument penetrating protons (Figure S.3, (*23*)).

The shape of the proton spectrum may be more complex than the power law we assumed. For example, an additional spectral break could exist at $\sim$100 MeV, where the efficiency of CRAND neutron production changes (*9, 31*). Such a spectral shape cannot be unambiguously constrained with just the two proton channels used here. Still, even if we pre-define its shape, the spectrum at $>$100 MeV remains hard, indicating that it may be possible to constrain the proton fluxes at the GeV range.

L-shell distribution of protons: The L-shell dependence of the differential proton fluxes at 300 MeV, deconvolved from their latitudinal and pitch angle dependencies, (Figure 4A) shows that the innermost proton belt peaks around L=1.1, just inward of the inner D-ring edge and in agreement with model predictions (*13*). That is a region where the combined material density from the D-ring dust and the atmospheric neutrals reaches a minimum, allowing the proton intensities to achieve the highest intensity levels.

The depth of the dropout attributed to the D68 ringlet has a clear pitch angle dependence. With decreasing α_{eq}, the depth of the absorption becomes less pronounced, as expected for

charged particles mirroring at high-latitudes, well away from where proton losses to dust occur. No absorption signature is resolved at the location of the D72 ringlet, even after the raw counts are processed and deconvolved of their latitudinal and pitch angle dependencies.

Low altitude ENA emissions and upper limits of <25 MeV proton, ion and electron fluxes: Upper limits for <25 MeV protons, 18-832 keV electrons and >5 MeV/nuc helium and oxygen are also included in Figures 3A,B. The results apply to L=1.1 but are similar within factors of three to all the L-shell range of the inner trapping region. The upper limits indicate a drop of the proton fluxes below about 25 MeV and negligible intensities for light or heavy ions. Evidence for the absence, or at least the lack of significant electron fluxes at any energy that LEMMS responds to (18 keV to ∼10 MeV) is provided in (*23*) (Figures S.4, S.5). In essence, the only resolvable trapped particle population with in-situ data comes from >25 MeV protons.

Even though MIMI did not observe keV protons in-situ, it detected remotely a 24-55 keV proton ENA emission from Saturn during its periapsis crossing on day 148/2017 (Figure 5). The proton population responsible for this emission must have resided below the lowest altitude of ∼3800 km sampled in-situ by MIMI on that day. The clear non-detection of ENAs in several other cases that INCA had the correct pointing to observe them (e.g. day 247/2017) suggests that the protons creating the ENA emission are transient.

Discussion

Origin of MeV protons from ring CRAND: Several lines of evidence verify that CRAND is the primary source process of the >25 MeV proton belt: the presence of protons, the extension of the spectrum well above 300 MeV, the lack of any resolvable signal from heavy ions and the temporal stability and the L-shell profile of the proton intensities. The L-shell profile (Figure 4) agrees qualitatively well with that derived from simulations (*13*), for which a CRAND source

was used as an input. Since this inner radiation belt is permanently decoupled from the rest of the magnetosphere, its detection alone constitutes one of the most direct observations of the CRAND process operating in our solar system.

In case of Saturn, CRAND may not only be catalyzed through the planet's atmosphere but also through the rings, from where we argue that the majority of CRAND protons that populate the inner radiation belt originate. One reason is that the rings have a significantly higher neutron yield than the planet's atmosphere (*31*). In addition, atmospheric neutrons that can reach the inner trapping region may only come off a latitude range below 36°, which is accessible to $>$40 GeV GCRs (*21*). Such GCRs have about four times lower integral flux than the $>$20 GeV GCRs which reach the main rings, that also offer a 50% larger neutron production area than the limited atmospheric zone. The attribution of the inner radiation belt source to ring CRAND is important for separating atmospheric and ring CRAND in the proton spectra of Saturn's main radiation belts, which has not been possible until now (*12, 17*).

Radiation belt and atmosphere coupling: The steep PAD inferred for both $>$25 MeV and $>$300 MeV protons inward of the D-ring ($L \lesssim 1.1$) can be attributed to energy losses of these protons to Saturn's extended atmosphere. We demonstrate this in Figure 4 by plotting the inverse value of the average atmospheric density encountered by protons of different pitch angles, as they move along the magnetic field (bounce-averaged atmospheric density), against the fluxes of 300 MeV protons. The inverse density profiles track the drop of the proton fluxes towards the planet, mostly for $L \lesssim 1.1$. In a similar way, the terrestrial atmosphere is responsible for very steep proton PADs in Earth's radiation belts (*32, 33*).

Radiation belt and D-ring coupling: For $L \gtrsim 1.1$, the inverse atmospheric density curves deviate from the deduced 300 MeV proton flux profiles, suggesting that the losses to the D-ring develop faster there. Using the D-ring density to proton flux scaling derived in (*13*), we estimate

that the D-ring column density needs to be below 10^{-8} g/cm^2 (*13*), which is orders of magnitude lower than the corresponding A and B-ring values (10-500 g/cm^2, (*34, 35*)). The partial, dust-driven depletion of the proton fluxes that we observe resembles the MeV proton interaction seen at Saturn's G-ring (L=2.71) (*17, 36, 37*). Because losses to D-ring dust are more significant for equatorially mirroring particles (α_{eq} $\sim$90°), they are likely responsible the reduced pitch angle anisotropy of protons compared (N$\sim$10) to the one observed at L$\lesssim$1.1 (N$\sim$100).

Despite that, the anisotropy at L$\gtrsim$1.1 remains large. The only remaining source of proton anisotropy may come from the CRAND process: since CRAND protons get injected along the direction of their parent, β-decay neutrons, their PAD may retain information about a preferential emission direction of neutrons from the rings. Simulations show that an isotropic, ring neutron emission would result to similarly isotropic proton PADs near the planet (*18*). The steep proton PAD at L$\gtrsim$1.1 may then be evidence that the neutron injection from the rings is highly anisotropic. Such an anisotropy may hold clues about the dust size distribution in Saturn's A-C rings, as it has been previously suggested (*9, 31*).

Diversity of the D-ring ringlets: Only two out of the three ringlets of the D-ring were shown to unambiguously influence the L-shell profile of the proton intensities (D68 and D73). D73 has a normal optical depth of $\sim 10^{-3}$ (*38*), which can be sufficient for depleting the energetic protons that LEMMS detects (*39*). D68 causes a strong reduction of proton fluxes (Figures 2, 4), while D72, which is as bright as D68, appears to have no impact on the trapped protons. This set of observations provides new insights on the diversity of the ringlets. The different influences of D68 and D72 on protons suggest that the former ringlet concentrates significant column mass in large grains and/or in its longitudinally confined arc, which has been observed remotely (*38*).

Comparison with Earth's radiation belts: Figure 3A shows the >25 MeV proton spectra from Saturn's inner trapping zone against those from L=1.4 in Earth's magnetosphere, where the proton belt fluxes above 100 MeV peak (*40*). The comparison indicates that Earth fluxes are about an order of magnitude higher for energies below 400 MeV. This difference is mostly due to solar protons, which can reach low L-shells at Earth through radial transport, a source not available at Saturn. A turnover occurs beyond ∼400 MeV and into the GeV range, where the projected proton fluxes at Saturn become stronger. Even though both Earth and Saturn produce CRAND protons in the GeV range, the 600 times stronger magnetic moment at Saturn allows a much more stable trapping of protons at relativistic energies (*29*). At Earth, trapped protons have been observed up to at least 2.2 GeV (*33*), while stable proton trapping is estimated to extend up to ∼5 GeV (*41*).

Comparison with Saturn's main radiation belts: It is interesting that proton fluxes in Saturn's main radiation belts drop more steeply with increasing energy (*11, 24, 42*) compared to what we infer for the innermost belt. Several explanations could account for this difference. Atmospheric CRAND in the main radiation belts, which can be generated by high flux, >0.5 GeV primary GCRs (*21*), is certainly more significant than it is closer to the planet. Magnetospheric radial diffusion becomes increasingly important at larger L-shells (*12*), where the proton trapping limit also drops to the range of ∼1 GeV. At this stage we cannot exclude that part of the difference seen in the spectra is due to the different LEMMS calibration used in the current and the past studies.

Electron CRAND and additional energetic particle sources: Our initial survey did not reveal any unambiguous signature of electrons (presumably from CRAND), at least below 837 keV. This suggests that even though CRAND produces electrons, these are lost more efficiently than protons and cannot not build up significant intensities. Since several studies indicate that

the CRAND source rates at Earth and Saturn are comparable (e.g. (*6*)), we can use this non-detection and make a rough-order-of-magnitude estimation for the time scales of CRAND electron losses in the inner belt.

If we assume that the rate that the 500 keV CRAND electron fluxes increase is 2.5×10^{-2}/(keV cm^2 sr s) in 1.5 hours, as measured at Earth (*20*), we find that CRAND electrons would exceed the upper detection limits shown in Figure 3B within just 1-2 days. That is a very short time compared to the expected, year-long trapping time scales of such particles that one would expect in the strong, axisymmetric magnetic field near Saturn. The non-detection indicates that 18-837 keV electrons are subject to losses which act faster than few days and could develop from electron scattering due to dust and neutrals, from wave-particle interactions, or even weak radial flows, to which electrons are much more sensitive that the protons (*43*). Such flows may drive CRAND electrons onto the C-ring or the atmosphere within few hours or days following their injection in the trapping region.

The very low upper limits for heavy MeV ions set tight constraints also on the intensity of other, non-CRAND related source process that may operate in this region, such as the local production of energetic light ions through elastic collisions of CRAND protons with atmospheric neutrals (*44*).

Low altitude, keV proton radiation belt: The transient character of the low altitude ENA emission confirms that its origin is in the variable ring current (*45*), as originally suggested (*2*). The 3800 km altitude limit inferred based on the lack of in-situ keV proton detection when the ENA emission image was obtained (Figure 5) can be further reduced to 2700 km, if we just rely on the value of the lowest L-shell that LEMMS had the appropriate pointing to observe these protons in-situ.

The difference with Jupiter is striking. There, keV protons which may have the same origin

(charge-stripped ENAs) have fluxes that are 3-5 orders of magnitude above the upper limits estimated for Saturn (*5*) (Figure 3A). It is possible that the highly structured internal magnetic field of Jupiter (*46*) enables ions produced through charge stripping in the denser layers of its upper atmosphere to follow drift shells which extend to higher altitudes, where the bounce-averaged density of neutrals that they become exposed to becomes negligible. That could allow ion fluxes to accumulate within less than a drift orbit around the planet and become detectable. The non-axisymmetric terrestrial magnetic field has a similar effect on CRAND electrons, as it allows them to accumulate only at a restricted longitude range where their drift orbit does not intersect the dense layers of our planet's atmosphere (*20*). The axisymmetric magnetic field of Saturn, on the other hand, restricts ions produced from charge stripping of ENAs to their high atmospheric density generation altitude, severely limiting their lifetime and the extension of their population to the L-shells where MIMI made its in-situ observations.

Conclusions

The Proximal orbits allowed the MIMI instrument to sample one of the few remaining unexplored regions of Saturn's magnetosphere and to complete one of the most comprehensive investigations of a planetary radiation belt other than Earth's.

MIMI measurements demonstrate that a radiation belt sector does indeed form inward of Saturn's dense rings, despite the isolation of this region from the rest of the magnetosphere and its collocation with dust and atmospheric neutrals. This radiation belt has two components. The primary one, bound by the planet's atmosphere and the D73 ringlet, originates from ring CRAND, comprises protons with energies extending for $\sim$25 MeV and into the GeV range and appears to be stable throughout the five month observation period. Its secondary, low altitude component was observed only remotely through ENA imaging, it is transient and contains protons of keV energies.

The strong coupling of the primary radiation belt component with Saturn's rings and atmosphere means that the MIMI measurements presented here will be central for achieving a quantitative description of the CRAND source strength by the main rings and the atmosphere, for probing the physical properties of Saturn's upper atmosphere, and for investigating the D-ring and its three ringlets. The non-detection of a signal from the keV proton population responsible for the ENA emission of the secondary belt, in the context of relevant measurements from Jupiter and Earth, highlights the importance of non-axisymmetric magnetic fields for the formation of low altitude radiation belts through multiple-charge exchange.

References and Notes

1. S. M. Krimigis, *et al.*, *Space Science Reviews* **114**, 233 (2004).

2. S. M. Krimigis, *et al.*, *Science* **307**, 1270 (2005).

3. J. F. Carbary, D. G. Mitchell, P. Brandt, E. C. Roelof, S. M. Krimigis, *J. Geophys. Res. (Space Physics)* **113**, 5210 (2008).

4. K. Dialynas, *et al.*, *J. Geophys. Res. (Space Physics)* **118**, 3027 (2013).

5. P. Kollmann, *et al.*, *Geophys. Res. Lett.* **44**, 5259 (2017).

6. J. A. van Allen, B. A. Randall, M. F. Thomsen, *Journal Geophys. Res.* **85**, 5679 (1980).

7. J. F. Cooper, *AAS/Division for Planetary Sciences Meeting Abstracts #40* (2008), vol. 40 of *Bulletin of the American Astronomical Society*, p. 460.

8. S. F. Singer, *Phys. Rev. Lett.* **1**, 181 (1958).

9. J. B. Blake, H. H. Hilton, S. H. Margolis, *Journal Geophys. Res.* **88**, 803 (1983).

10. R. S. Selesnick, M. K. Hudson, B. T. Kress, *J. Geophys. Res. (Space Physics)* **118**, 7532 (2013).

11. E. Roussos, *et al.*, *J. Geophys. Res. (Space Physics)* **116**, A02217 (2011).

12. P. Kollmann, E. Roussos, A. Kotova, C. Paranicas, N. Krupp, *Nature Astronomy* (2017).

13. P. Kollmann, *et al.*, *J. Geophys. Res. (Space Physics)* **120**, 8586 (2015).

14. M. M. Hedman, *et al.*, *Icarus* **188**, 89 (2007).

15. M. M. Hedman, *et al.*, *Icarus* **199**, 378 (2009a).

16. M. Hedman, J. Burt, J. Burns, M. Showalter, *Icarus* **233**, 147 (2014).

17. P. Kollmann, E. Roussos, C. Paranicas, N. Krupp, D. K. Haggerty, *Icarus* **222**, 323 (2013).

18. J. F. Cooper, *Journal Geophys. Res.* **88**, 3945 (1983).

19. R. Srama, *et al.*, *Space Science Reviews* **114**, 465 (2004).

20. X. Li, *et al.*, *Nature* **552**, 382 (2017).

21. A. Kotova, Energetic particle tracking techniques and its application to the magnetosphere of Saturn, Theses, Uninersite Toulouse III – Paul Sabatier (2016).

22. I. G. Usoskin, K. Alanko-Huotari, G. A. Kovaltsov, K. Mursula, *J. Geophys. Res. (Space Physics)* **110** (2005). A12108.

23. Materials and methods are available as supplementary materials at the Science website.

24. T. P. Armstrong, *et al.*, *Planet. Space Sci.* **57**, 1723 (2009).

25. E. Roussos, *et al.*, *Geophys. Res. Lett.* **(this issue)** (2018).

26. J. A. Van Allen, M. F. Thomsen, B. A. Randall, R. L. Rairden, C. L. Grosskreutz, *Science* **207**, 415 (1980).

27. S. M. Krimigis, T. P. Armstrong, *Geophys. Res. Lett.* **9**, 1143 (1982).

28. R. E. Vogt, *et al.*, *Science* **215**, 577 (1982).

29. T. J. Birmingham, *Journal of Geophysical Research* **87**, 7421 (1982).

30. M. F. Thomsen, J. A. Van Allen, *Journal Geophys. Res.* **85**, 5831 (1980).

31. J. F. Cooper, R. E. Johnson, P. Kollmann, E. Roussos, E. C. Sittler, *Plasma, Neutral Atmosphere, and Energetic Radiation Environments of Planetary Rings*, Cambridge Planetary Science (Cambridge University Press, 2018), p. 363–398.

32. R. S. Selesnick, *et al.*, *J. Geophys. Res. (Space Physics)* **119**, 6541 (2014).

33. O. Adriani, *et al.*, *ApJ* **799**, L4 (2015).

34. S. J. Robbins, G. R. Stewart, M. C. Lewis, J. E. Colwell, M. Sremčević, *Icarus* **206**, 431 (2010).

35. J. E. Colwell, *et al.*, *Saturn from Cassini-Huygens*, Dougherty, M. K., Esposito, L. W., & Krimigis, S. M., ed. (Springer Science+Business Media B.V., Heidelberg, Germany, 2009), p. 375.

36. J. A. Van Allen, *Journal Geophys. Res.* **88**, 6911 (1983).

37. M. M. Hedman, *et al.*, *Science* **317**, 653 (2007).

38. M. M. Hedman, *et al.*, *Icarus* **188**, 89 (2007).

39. C. Paranicas, A. F. Cheng, *Icarus* **125**, 380 (1997).

40. R. S. Selesnick, D. N. Baker, S. G. Kanekal, V. C. Hoxie, X. Li, *J. Geophys. Res. (Space Physics)* .

41. R. S. Selesnick, M. D. Looper, R. A. Mewaldt, *Space Weather* **5** (2007). S04003.

42. P. Kollmann, *et al.*, *J. Geophys. Res. (Space Physics)* **116**, A05222 (2011).

43. E. Roussos, *et al.*, *Icarus* **305**, 160 (2018).

44. R. S. Selesnick, R. A. Mewaldt, *J. Geophys. Res. (Space Physics)* **101**, 19745 (1996).

45. S. M. Krimigis, N. Sergis, D. G. Mitchell, D. C. Hamilton, N. Krupp, *Nature* **450**, 1050 (2007).

46. J. E. P. Connerney, *et al.*, *Geophys. Res. Lett.* **45**, 2590 (2018).

47. W. R. Johnston, T. P. O'Brien, S. L. Huston, T. B. Guild, G. P. Ginet, *IEEE Transactions on Nuclear Science* **62**, 2760 (2015).

Acknowledgments: The authors like to thank M. Gkioulidou (JHU/APL) and J. Cooper (GSFC) for useful discussions, Andreas Lagg (MPS) and Jon Vandegriff (JHU/APL) for extensive software support and Martha Kusterer (JHU/APL) for reducing the MIMI data. **Funding:** The German contribution of the MIMI/LEMMS Instrument, ER and NK were in part financed by the German BMWi through the German Space Agency DLR under contracts 50 OH 0103, 50 OH 0801, 50 OH 0802, 50 OH 1101, 50 OH 1502 and by the Max Planck Society. The JHU/APL authors were partially supported by the NASA Office of Space Science under task order 003 of contract NAS5-97271 between NASA/GSFC and JHU. GHJ is partially supported by the UK Science and Technology Facilities Council. French participation in the Cassini project (AK and ID) is funded by CNES. LHR contribution was supported by a NASA Living With a Star grant (NNX16AL12G). BP is supported by the PRODEX program managed by ESA in collaboration

with the Belgian Federal Science Policy Office. **Author contributions:** All authors contributed to the discussion and interpretation of the data and the writing of the manuscript. ER and PK performed most data analysis tasks. ER updated the LEMMS sensor in-flight calibration and performed the response simulations. PK developed and applied the inversion method to obtain proton spectra and PADs. AK and LR evaluated the importance of CRAND anisotropy. GHJ constructed the graphics for Figure 1 and the Figure of the extended abstract. **Competing interests:** The authors declare no conflicts of interest **Data and materials availability:** The Cassini/MIMI data and a user guide are available online through NASA's planetary data system (PDS - `https://pds.nasa.gov/`). All raw MIMI data shown here will be released via the PDS within 2018.

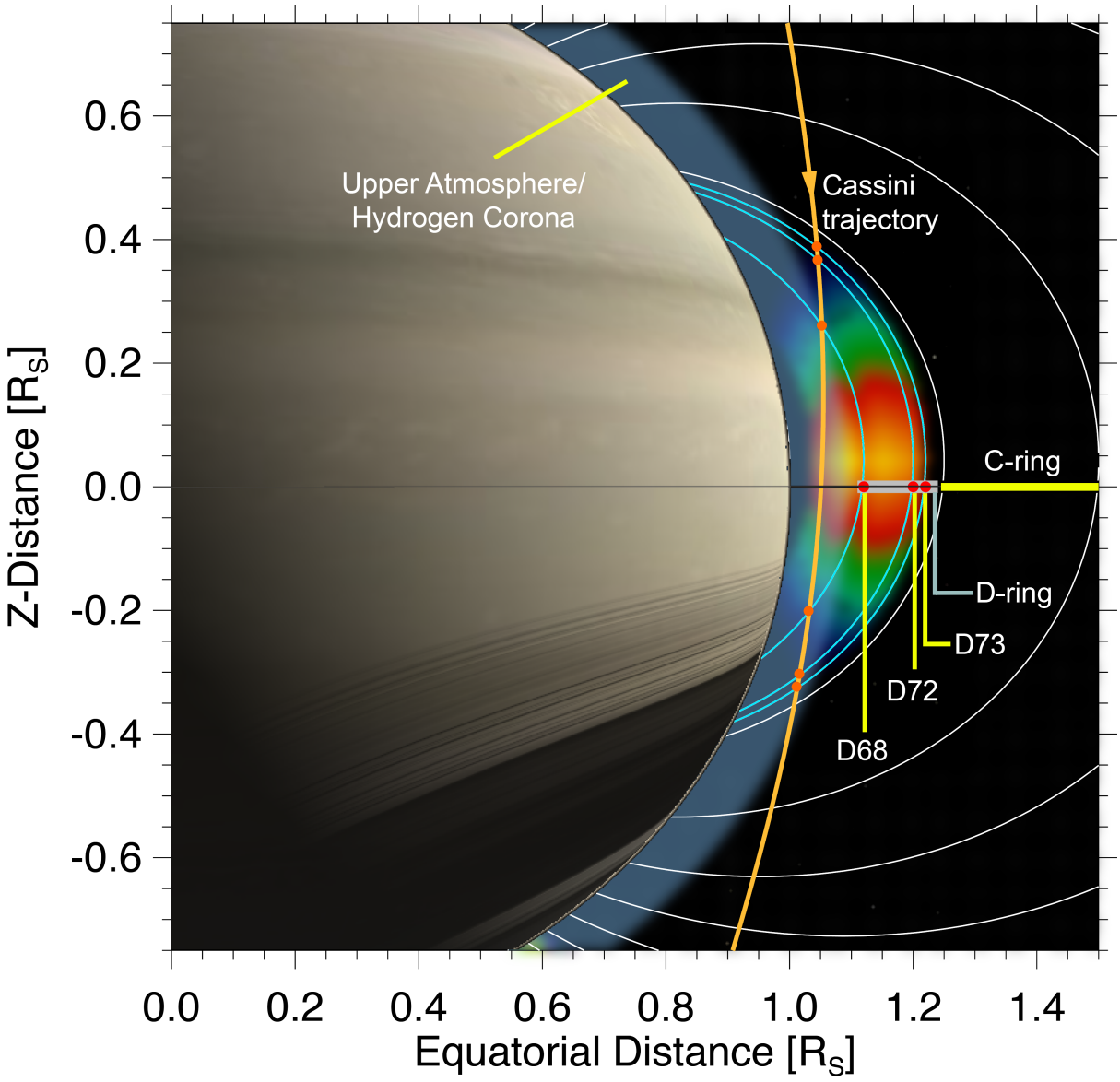

Figure 1: **The geometry of the energetic particle trapping region between Saturn's rings and atmosphere.** This region is indicated by the color map, which is based on the radial proton flux profile shown later in Figure 4. A typical Cassini Proximal orbit trajectory is shown in orange. Cassini first intersects this region at about 20° north latitude and exits at a similar latitude to the south. As trapped particles move along the magnetic field, Cassini can probe the effects of the D-ring's dust environment from high-latitudes, without directly crossing through it. The orange circles mark the locations along Cassini's trajectory where the effects of the D-ring's ringlets (D68, D72, D73) on the trapped particle population can be can be transmitted along the magnetic field lines drawn in light blue. Other field lines (in white) are drawn every 0.25 R_S at the equatorial plane.

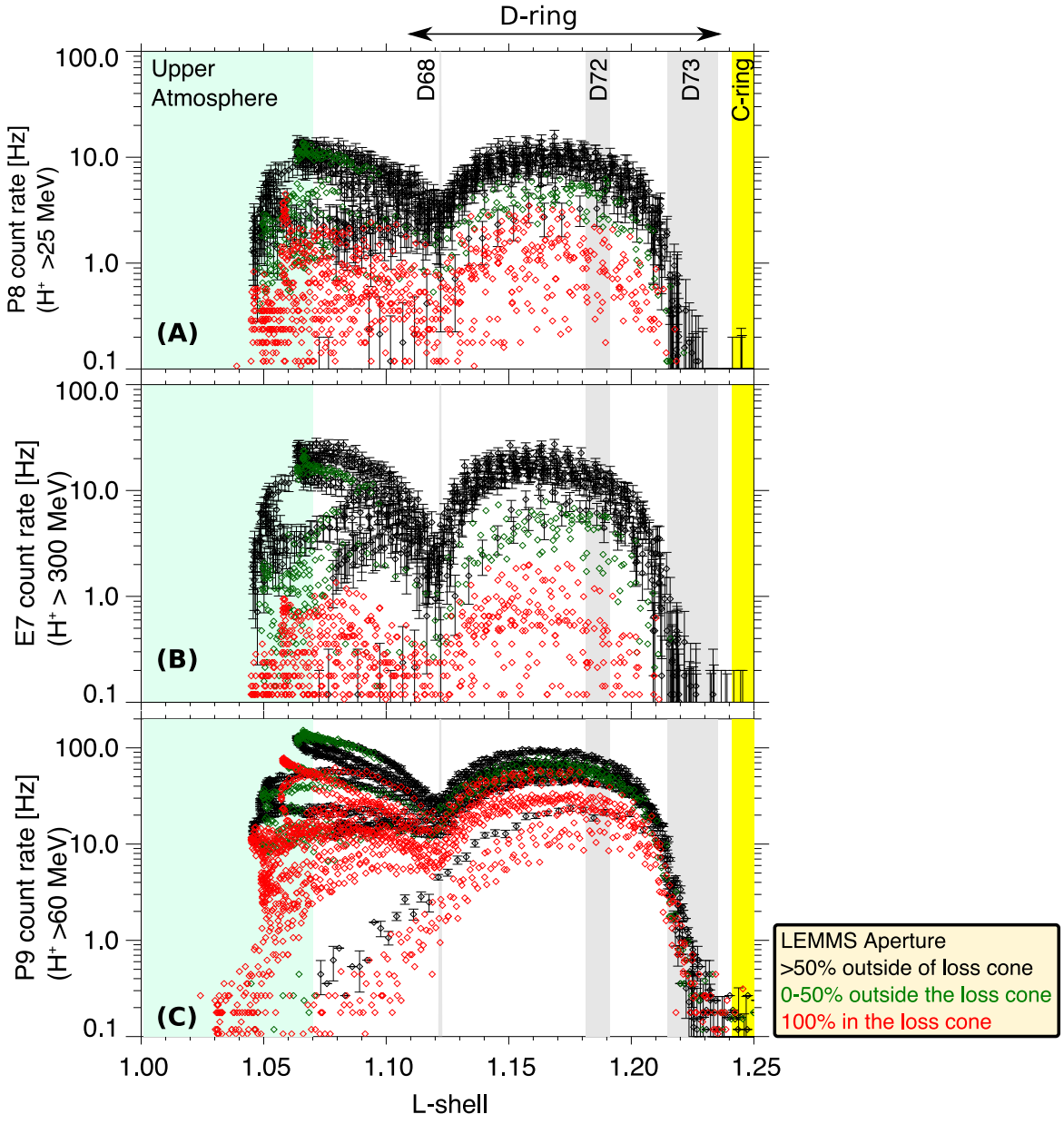

Figure 2: **MIMI/LEMMS count-rates as a function of the L-shell**. Data are obtained from all the proximal orbits (April 23 - September 15, 2017) and for regions mapping magnetically inward of Saturn's C-ring. All channels shown are dominated by protons and cover the energy range above 25 MeV. Count rates are averages of three consecutive samples (one data point per $\sim$16 s). The points are color-coded according to the percentage of LEMMS's aperture within the planetary loss cone, as explained in the legend right of Panel (C). It can be seen that the channels in the upper two panels roughly organize with pitch angle, while the channel in the lower panel, representative of most other LEMMS channels not shown here, does not, due to its high-sensitivity to sideways, instrument penetrating protons.

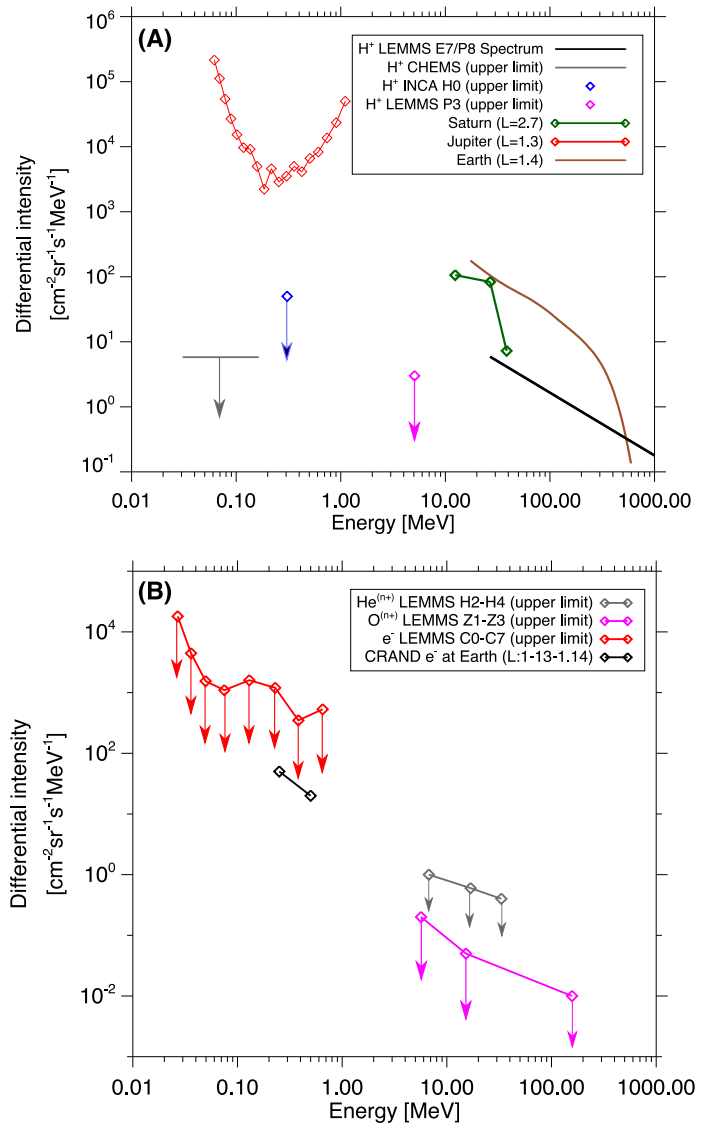

Figure 3: **Energetic particle spectra and upper limits.** Panel A includes a preliminary proton spectrum of 25 MeV to >1 GeV protons (black line). As the PAD of the 25 MeV to ∼1 GeV protons is highly anistotropic, a pitch-angle averaged spectrum is plotted. All other symbols denote upper flux limits for lower energy protons. For comparison, we also show a proton spectrum from L=1.3 at Jupiter (*5*), from L=2.4 at Saturn (*11*) and from L=1.4 (α_{eq} ∼90°) at Earth (*40*). Panel B shows upper flux limits for ions and electrons. The H2-H4 and Z1-Z3 channels can only constrain the minimum atomic mass numbers of the ions detected (Z≥2 and Z≥8, respectively) but we assume these are helium and oxygen. On the horizontal axes, units for protons and electrons are in MeV, for ions in MeV/nuc. The upper limits of electron fluxes can be compared against the maximum electron CRAND fluxes measured at the Earth, based on (*20*). All Saturn innermost belt measurements are from L=1.1.

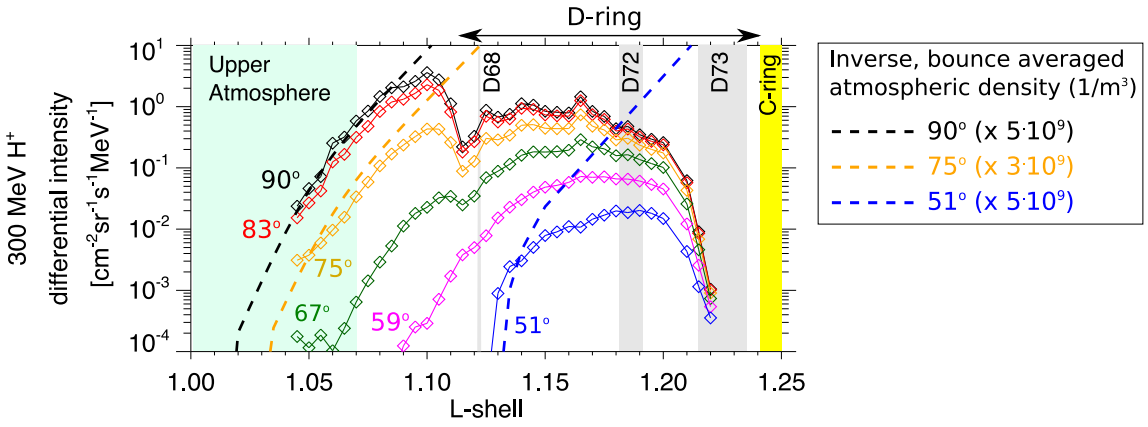

Figure 4: **The L-shell dependence of 300 MeV proton differential intensities**. Different lines and colors correspond to different α_{eq}. Intensities are only shown where the inversion was successful. The progressively smaller extension of the radiation belts for decreasing pitch angles is due to the increasing size of the loss cone towards lower L-shells. The small offset of the central dropout from the L-shell of D68 is probably due to systematic errors associated with the magnetic field model used in this study. Overplotted are three curves showing the inverse of the bounce-averaged atmospheric density (*13*), scaled by appropriate factors for a better comparison with the proton fluxes. The small difference in the adopted scaling factors is due to the imperfect atmospheric model used.

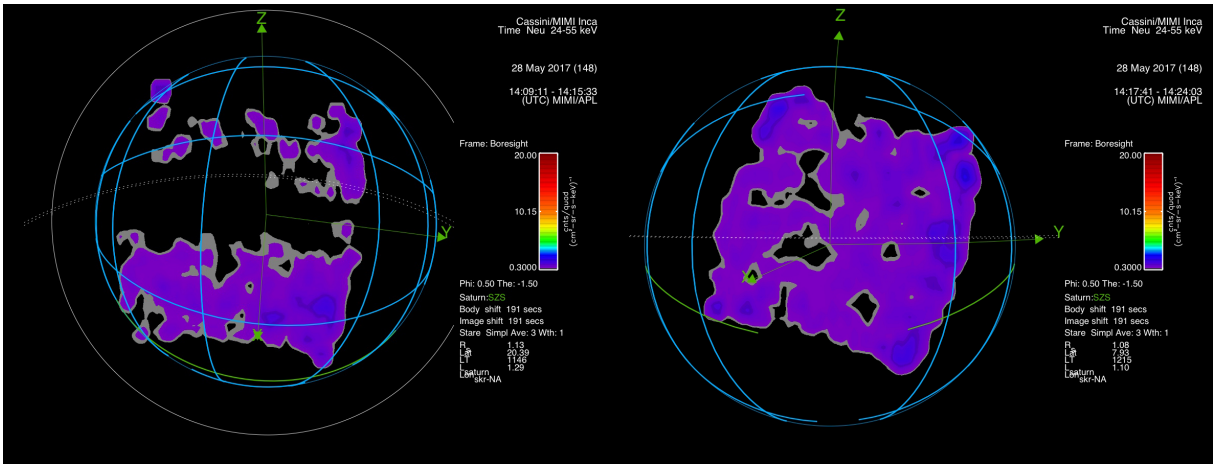

Figure 5: **Imaging of the low altitude ENA emission.** Images of Saturn in 24-55 keV proton ENAs obtained with the MIMI/INCA camera on May 22, 2017. The two frames are taken from the same sequence, with a time difference of 8 minutes. The emission is from the low-altitude keV ion radiation belt, observed also at SOI in 2004 (*2*). The boundaries of the emission are due to INCA's field of view. The coordinate system displayed has its origin at the center of Saturn, with the z-axis pointing north, the y-axis towards dusk and along Saturn's equatorial plane, while the x-axis completes the right-hand system, pointing approximately towards the Sun.

SUPPLEMENTARY MATERIALS

Materials and Methods

- Latitudinal and pitch angle dependencies of proton rates
- MIMI/LEMMS responses
- Species Identification
- Relating Instrument Counts and Intensities

Figures S1-S6

References 48-59

Materials and Methods

Latitudinal and pitch angle dependencies of proton rates

Figure S1.A shows the L and α_{eq} distribution of $>$300 MeV proton count rates averaged over the 22 Proximal Orbits. The features described below apply also to the measurements of $>$25 MeV protons. The averaged rates tend to increase towards α_{eq}=90° for most of the L-shell range of the trapping region. Simultaneously, count rates experience an increase towards lower magnetic latitudes (Figure S1.B). The latitudinal and pitch angle slopes are very steep: count-rates change by an order of magnitude within just $\sim$5° of latitude or $\sim$15° of α_{eq} (Figure S.6, (*23*)).

MIMI/LEMMS responses

In this section we describe new simulations of the LEMMS geometry factors and the procedures that are necessary for the conversion of the raw measured count rates (as in Figure 2) into differential intensities (as in Figures 3 and 4). The harsh environment of the innermost radiation

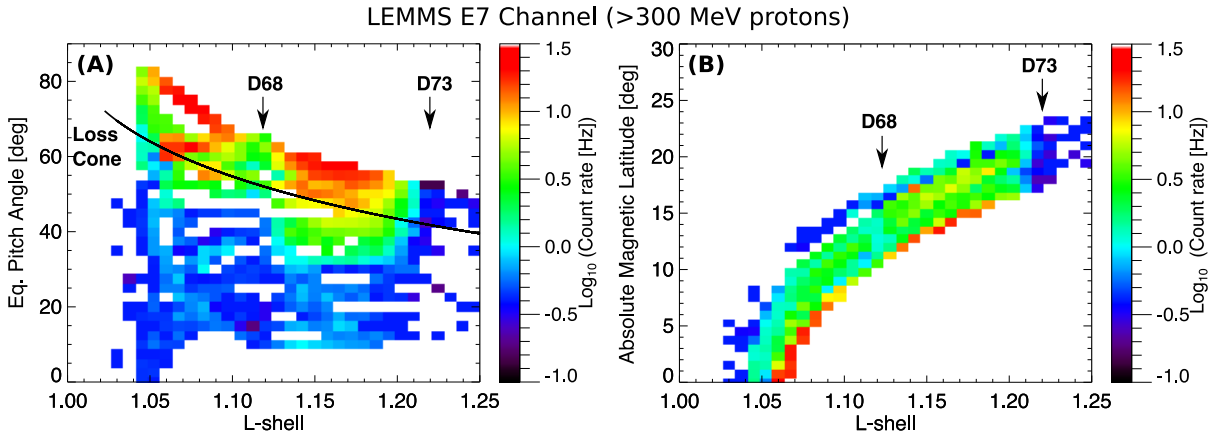

Figure S.1: **Count-rate spectrograms as a function of L-shell, pitch angle and latitude.** Panel (A): L-shell vs. α_{eq} spectrogram of >300 MeV proton count-rates, averaged from all Cassini's Proximal Orbits. The boundary of the loss cone is overplotted with a black line. Panel (B): L-shell vs. Absolute magnetic latitude spectrogram of >300 MeV proton count-rates.

belts as well as the opportunity to resolve the loss cone (and therefore directly separate penetrating radiation from foreground) made us revisit the previous calibration, for which it was assumed that contribution of instrument penetrating radiation was negligible. The simulations described below are vital to interpret the data presented in this paper and would likely improve our understanding of the radiation belts outward of the main rings.

LEMMS simulation setup: The response simulations of LEMMS were carried out using the GEANT4 Radiation Analysis for Space (GRAS) software (*48, 49*). GEANT stands for "Geometry and Tracking". We constructed a 3d-model of LEMMS using the Geometry Description Markup Language (GDML). The design, including material assignment to the different volume elements, was based on archived mechanical drawings of the instrument.

The model that we constructed comprises the three main parts of LEMMS: the sensor, the housing of electronics, and the scan platform (Figure S2.A). It includes most of the sensor's key details, namely the distribution of passive shielding by heavy and light material, the geometry

of the collimator, and the positions and sizes of the solid state detectors (SSDs). The implementation of the other two elements (electronics and scan platform) is much simpler but sufficient (Figure S2, panels B-D). The model mass is 6.45 kg, or 95% of the actual mass of LEMMS (6.72 kg). The Cassini spacecraft was not included in these simulations.

In the LET, separation of electrons and ions is caused by the use of a permanent magnet, which directs electrons away from the telescope axis and onto detectors E1 and F1. The volume and the materials of the magnetic assembly (soft iron, samarium-cobalt magnets) are prescribed in the model, but the magnetic field was not included since we simulated $>$1 MeV protons, the trajectories of which are not affected by it.

Geometry factor derivation: The output of the GEANT4/GRAS simulations was used to provide the geometry factors of LEMMS as described below. We injected $1.5\,10^9$ 1 MeV - 5 GeV protons from a spherical surface of radius r=17 cm surrounding the instrument model. A cosine angular distribution was chosen for the source protons. For each proton event we recorded the ionizing energy losses on the various LEMMS SSDs and applied the coincidence logic described in (*1*) in order to obtain the geometry factor, G, for any the instrument's 56 channels, through the following Equation 1 (*50*):

$$G = 4\pi^2 r^2 \frac{N_C}{N_I} \tag{1}$$

N_C is the number of proton events satisfying a channel's coincidence logic, and N_I the number of injected particles. By binning N_C and N_I over energy, we can obtain the energy dependence of the geometry factor, $G(E)$.

Equivalent to G, we define g_d, as the differential geometry factor, practically the effective detector area that the protons see if they are injected from within an angular interval of $\theta_1 < \theta < \theta_2$, where θ is the angle between the LEMMS boresight and the proton velocity vector at

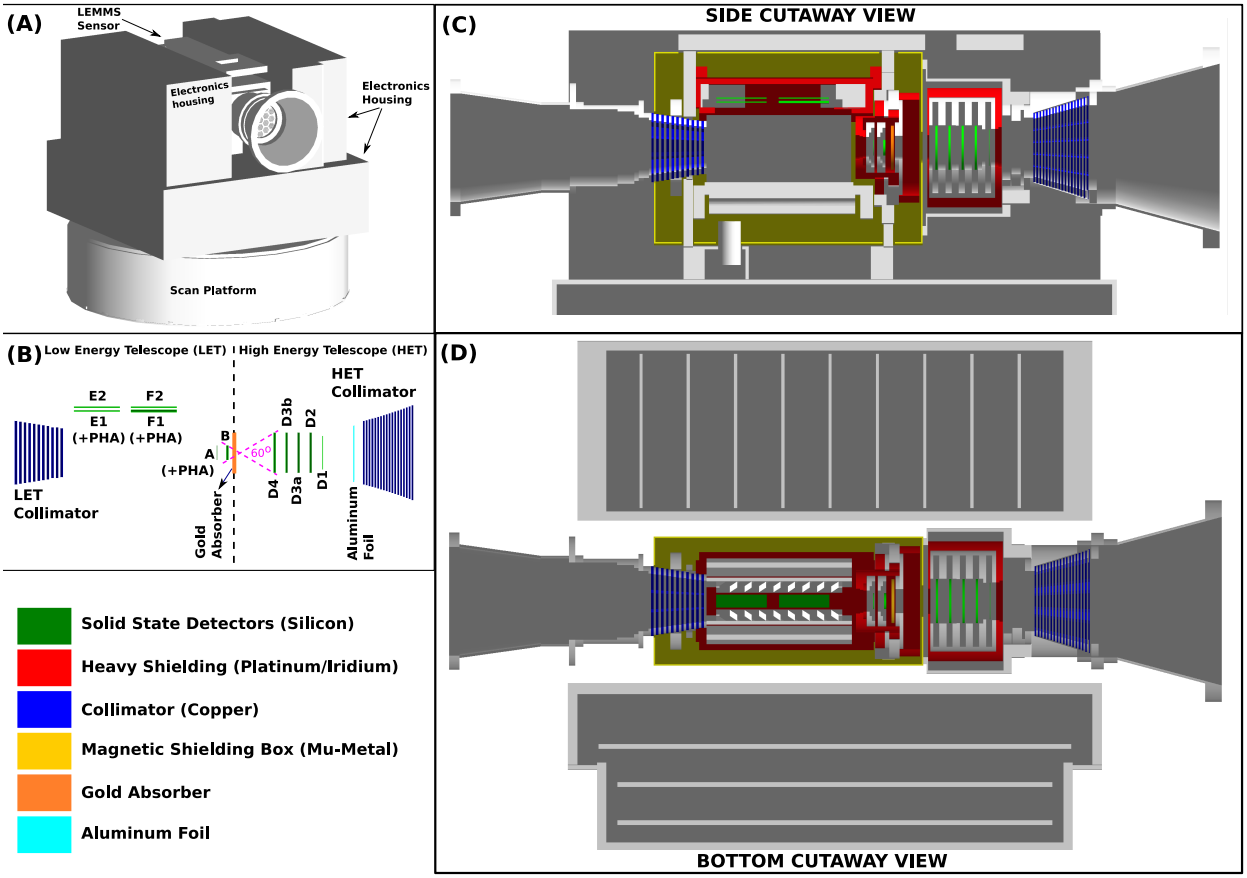

Figure S.2: The LEMMS 3d-model used for response simulations with GEANT4/GRAS. Panel (A): Perspective view of the LEMMS model from the side of the High Energy Telescope (HET). Panel (B): The detector geometry of the LEMMS sensor. Blue lines show the disks that make up the volume of the collimator. The collimators have holes to allow particles to pass. Labels as A, E1, D3a are detector names. Detectors that can perform pulse height analysis measurements (PHA) are also indicated. Electrons reach the E and F detector assembly after being deflected by a permanent magnet within the LET. The opening of the LEMMS collimators is 15°(LET) and 30°(HET). Penetrating particles cannot be collimated and the acceptance angle is greater (e.g. 60° for coincident measurements in the B and D4 detectors - magenta lines). Panels (C) and (D): Side and bottom cutaway views of the LEMMS instrument. The color-coding is explained in the bottom-left side of the figure. Grey volumes are of light material (e.g. aluminum, polyimide for the electronic boards etc.)

the source. In that case:

$$g_d = \frac{g}{\Delta\Omega} = \frac{\pi r^2}{(\cos\theta_1 - \cos\theta_2)} \frac{N_c}{N_I} \tag{2}$$

where N_c is the number of proton events with $\theta_1 < \theta < \theta_2$ satisfying a channel's coincidence logic. For simplicity we replaced all θ >90° with 180°-θ, so that g_d becomes the total geometry factor of HET and LET combined. An equivalent expression to Equation 2 can be found in (*40*) (their Equation 2). Values for G are shown in Figure S.3A, while for g_d in Figure S.3 (panels B-D).

Discussion of the instrument response: Our simulations validated the energy passbands of LEMMS channels P1-P6 (HET) between 1.4 and 13.4 MeV, that have been used in the previous calibration (*24*). The geometry factor for all these channels was calculated to be 0.054 cm^2sr. This number is slightly higher than the one assumed in the previous LEMMS team calibration (0.040 cm^2sr). The small difference is due to an improved model of the collimator.

For channels P7-P9, which monitor higher energy protons, their calibration requires significant updates. These channels capture protons penetrating the collimator (>35 MeV) and the shielding (>60 MeV) and that increases those channels' acceptance angle and geometry factors and broadens their energy passbands. Our simulations allowed us to also obtain the proton responses of LEMMS's E-channels above 100 MeV, especially for channel E7 that we rely on here for our analysis. The E-channels were designed and so far used to monitor electrons (e.g. (*42*)).

Results for LEMMS channels P8, P9, and E7, the data of which are plotted in Figure 2, are shown in Figure S.3. We can use these simulation results to provide context for the LEMMS measurements. More specifically:

- The simulations suggest that E7, a channel designed to measure electrons, can also mea-

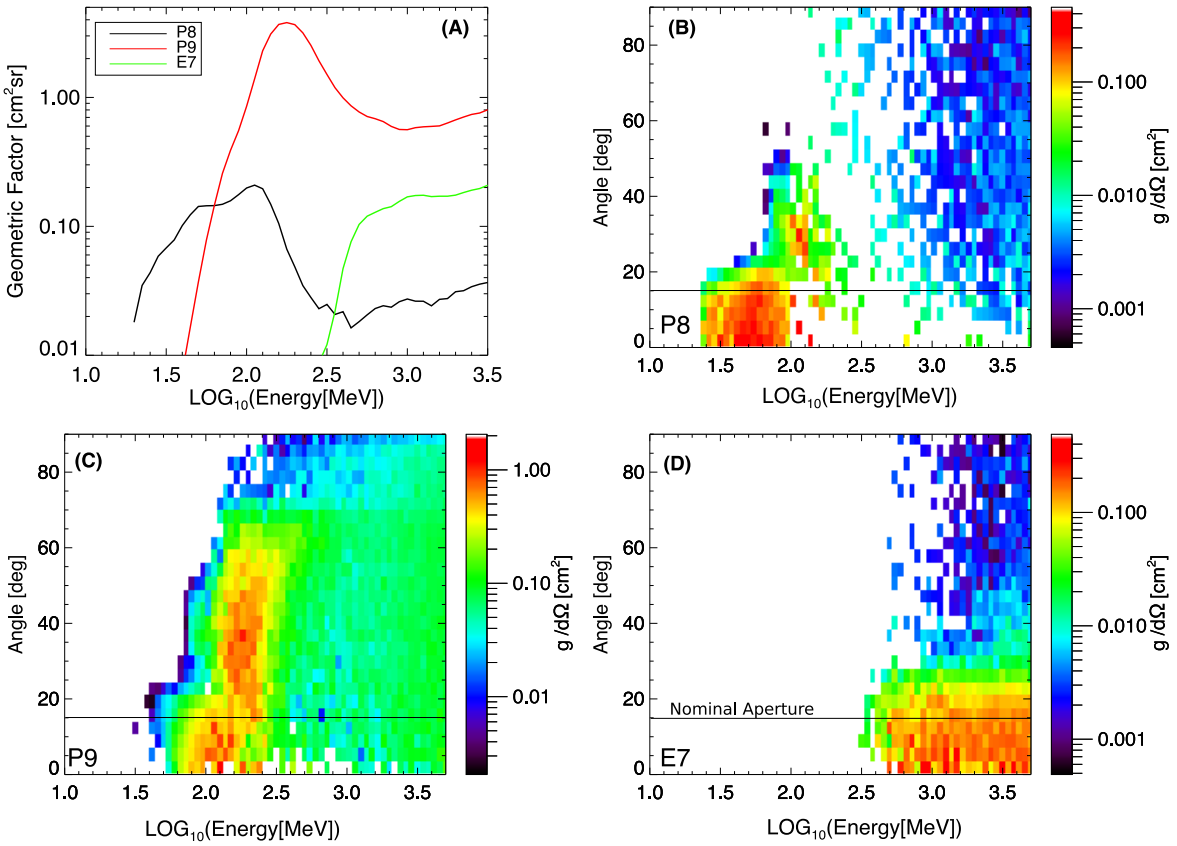

Figure S.3: Results of the proton response simulations for LEMMS channels P8, P9, and E7. Panel (A): Omnidirectional geometry factors G as a function of incident proton energy. Panels (B)-(D): Differential geometry factors g_d as a function of proton energy and incidence angle (θ) with respect to the LEMMS LET or HET boresight. The black horizontal line marks the geometric half opening angle of the HET.

sure protons at energies much higher ($>$ 300 MeV) than any of LEMMS's nominal proton channels . A confirmation of this finding with in-flight data is shown in the next subsection of the appendix and Figure S.4. The detector geometry is such that E7 should count protons coming within an acceptance cone of 60° (or 30° half-angle) (Figure S.2B) with respect to the telescope axis. That is very close to the $\sim$25° half-angle where E7 has its highest sensitivity based on the simulations (Figure S.3D). The gold absorber between B and D4 limits accidental coincidences by scattered secondaries of high energy protons penetrating at large angles.

- P8 has an efficient coincidence logic for rejecting penetrating particles, except for the energy range between about 80 and 150 MeV, where a strong secondary response is seen to protons with 25° $< \theta <$50°. That explains why this channel gets more noise from sideways penetrating radiation than E7.

- P9 has a relatively large geometry factor at all proton energies that it responds to (Figure S.3A). That explains why its count rate is about an order of magnitude higher than those of E7 and P8 (Figure 2C). The relatively high geometry factor of P9 is due to its large sensitivity to sideways penetrating particles: a very strong response is seen for penetrating 100-300 MeV protons with incident angles up to 65°. The sensitivity remains high for all angles even above 300 MeV. That clarifies why count rates of P9 in and out of the loss cone are very similar (Figure 2C).

Species Identification

MIMI/LEMMS observations during Cassini's Earth flyby: An opportunity to validate the double species response of LEMMS channel E7 with in-flight data is offered through the measurements obtained during Cassini's Earth flyby on August 18, 1999 (day 230/1999). Cassini's

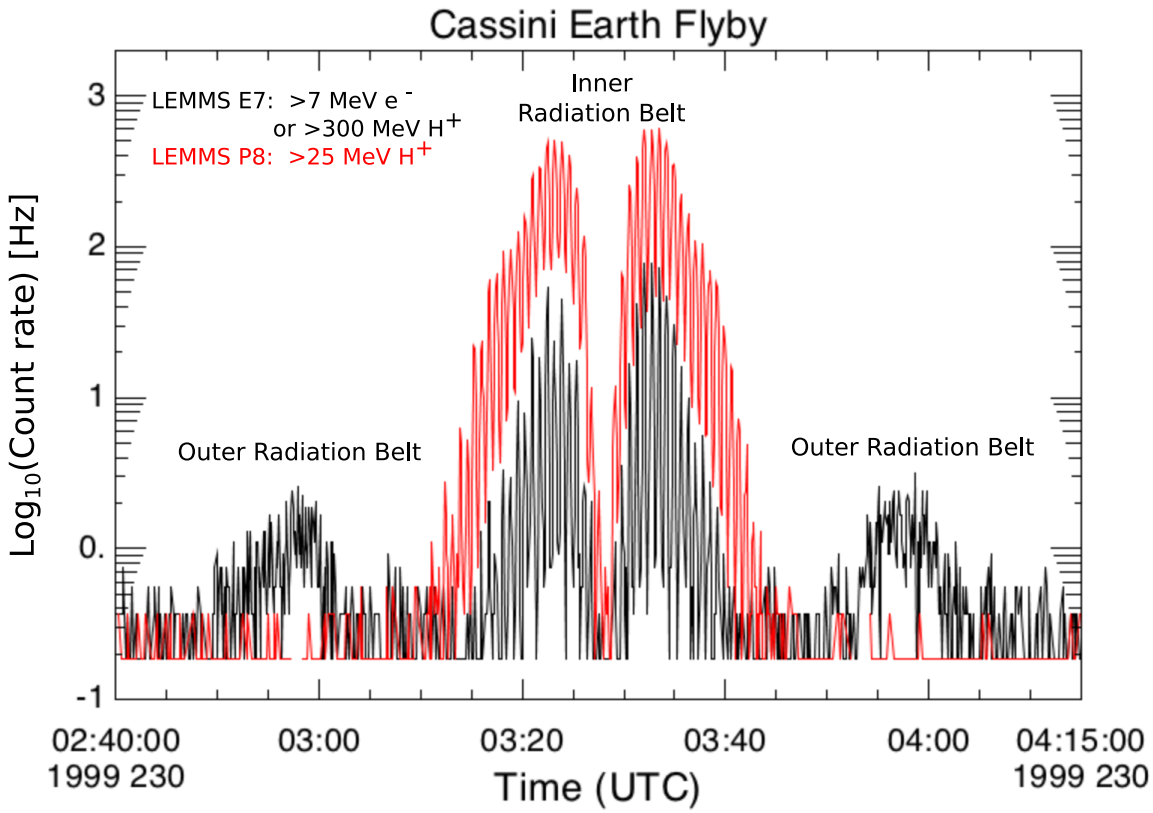

Figure S.4: LEMMS measurements during the periapsis of Cassini's Earth flyby on August 18, 1999. The rates of two channels are plotted, E7 and P8. The former has a double species response while P8 is a clean MeV proton channel. The periodic modulation of the signal is due to the rotation of LEMMS through its scan platform.

closest approach to Earth was 7542 km from its center (or 1.18 Earth radii with 1 $\mathrm{R_E}$=6371 km) and LEMMS data from its crossing through the Van Allen radiation belts are shown in Figure S.4. Channels E7 and P8 get their peak count rates near the periapsis around 03:27 UTC, when LEMMS was sampling the inner radiation zone. Recent observations showed that this region is dominated by MeV protons, while electron fluxes above 1-2 MeV are negligible (***?, ?, ?***). Since the E7 channel is sensitive to even higher energy electrons ($>$7 MeV), its signal between 3:15 and 3:45 can only be explained if it also responds to protons, in agreement with what the detector simulations indicate. The similarity with the profile of the proton channel P8 for this 30 minute time period also supports this conclusion. The periodic modulation of the signal in these two channels is due to changes in the pitch angle pointing of LEMMS, as its scan platform was operational at that time. The modulation of E7 and P8 signals is in phase, as expected for protons of that region with the characteristic energies measured by these two channels, which have a similar PAD shapes (*32*).

The E7 channel detects a foreground signal also on 02:50-03:05 and 03:50 - 04:05 UTC. In this case, the E7 counts come from $>$7 MeV electrons of the outer radiation belt (*47*) rather than protons: the absence of protons is demonstrated by the channel P8, which is at background. These measurements confirm that E7 is a dual-species channel.

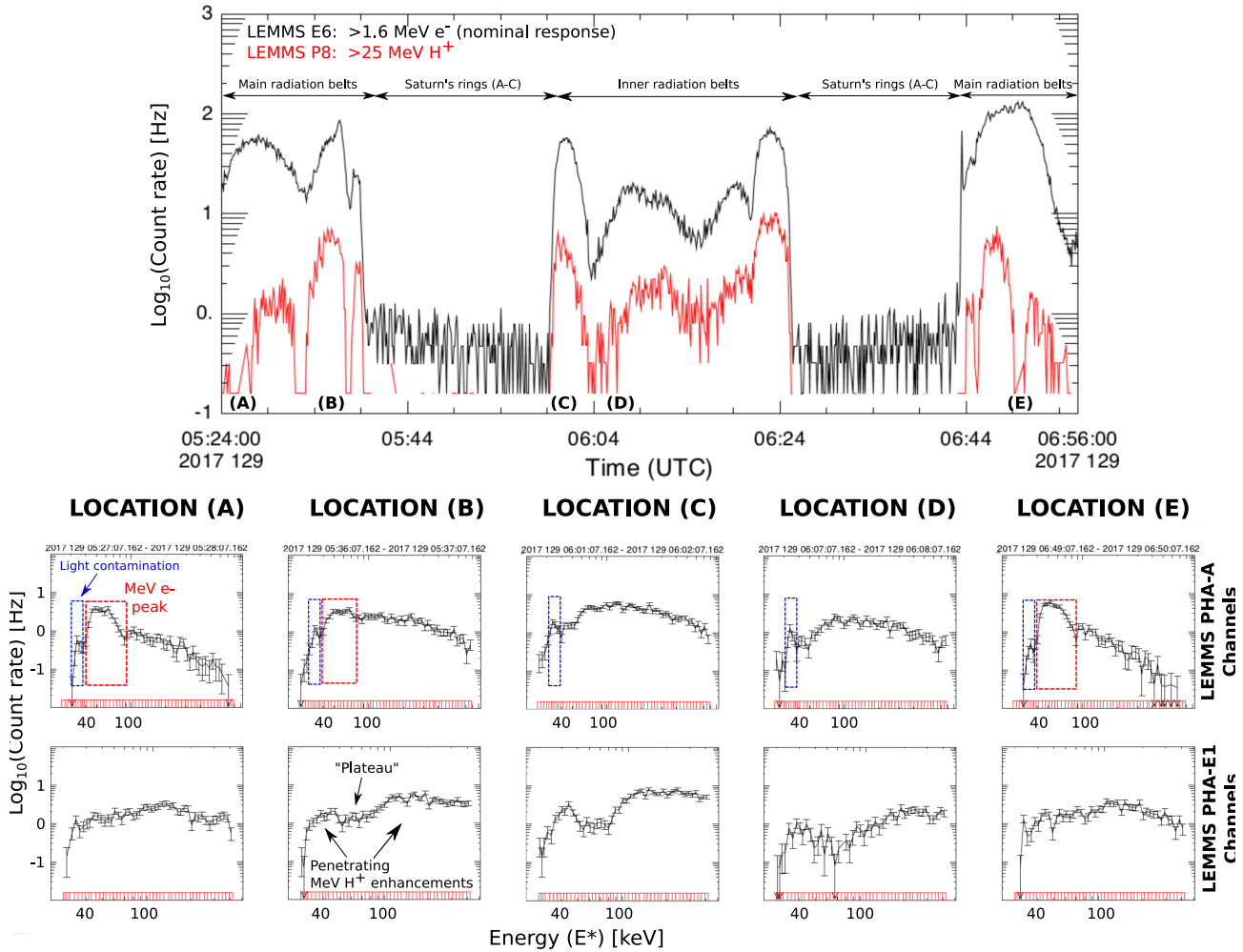

Figure S.5: Top: Time series of LEMMS measurements during the periapsis of Cassini's third proximal orbit (day 129/2017). The rates of two channels are plotted, E6 and P8. The former has a double species response while P8 is a clean MeV proton channel. Several locations (A-E) are marked above the time-axis. Bottom panels: High-resolution PHA spectra at locations A-E, from LEMMS detectors A (top row) and E1 (bottom row). Several spectra features are highlighted and explained in the text. The count-rate spectra are plotted as a function of energy. The energy bins are shown with red on the horizontal axes. We refer to energy as "pseudo-energy" (E^*) since detector counts for the specific interval are due to instrument penetrating particles, for which the correspondence between the pulse-height they cause on the A and E1 detectors and the particles' primary energy is not valid.

High energy resolution spectra of instrument penetrating radiation: LEMMS achieves high energy resolution particle spectroscopy by applying Pulse Height Analysis (PHA) to the SSD signals. Figure S2.B shows the location of SSDs E1, F1 and A on the LET where PHA spectra can be obtained for energies below 1.2 MeV for electrons (E1 and F1) and 800 keV for ions (A). In the innermost radiation belts, where fluxes of such particles are negligible (e.g. Figure 3), the PHA detectors provide us with high energy resolution spectra of instrument penetrating particles and their secondary products. We analyze these spectra and find that the intensity of energetic electrons in the innermost radiation belts is likely low.

Even though the three detectors are positioned within few cm of each other, the shielding distribution around them is different. Furthermore, low energy secondary particles generated in their vicinity may be preferentially focused to certain detectors due to the presence of LET's permanent magnets. As a result, each PHA detector shows a variety of features which we can associate to MeV protons, MeV electrons, or a combination of these two populations.

In the top panel of Figure S.5 we show time series of count-rates from LEMMS channel E6 (nominally $>$1.6 MeV electrons) and P8 ($>$25 MeV protons) obtained during Cassini's periapsis of the third proximal orbit (day 129/2017). PHA spectra from detectors A and E1 are shown from five time intervals marked on the bottom of that plot (locations A-E). The spectra show count rates as a function of "pseudo-energy", E^*. We call this pseudo-energy because the plotted PHA energy values correspond to the energy that a foreground population of $<$800 keV protons and $<$1.2 MeV electrons would have had in order to trigger the A and E1 detectors, respectively.

At locations (A) and (E), Cassini samples Saturn's electron radiation belt outside of the main rings. At both locations penetrating radiation is dominated by MeV electrons. MeV protons are absent, as they have been fully absorbed by Enceladus and Mimas, respectively (*51*). In that case, a characteristic peak at 40$<$ E^* $<$80 keV and a power-law drop-off at higher

pseudo-energies is visible in the PHA-A spectra. In the absence of protons, this signature can be attributed with certainty to MeV electrons. We will search below for such a signature within the innermost belt. In the E1 detector, the pseudo-energy spectrum from MeV electrons is relatively flat with a broad peak centered around 110 keV.

Location (B) is still within the main radiation belts, but in a region where both MeV protons and electrons have high contributions. Any qualitative differences with respect to the spectra from locations (A) and (E) are due to MeV protons. We can see that the MeV electron peak in PHA-A is still resolvable, but it is less pronounced because it is superimposed on a count-rate increase from MeV protons in the same E^* range. For E^* >80 keV, the protons make the spectrum flatter and the steep power-law drop-off of the electrons is not visible. In the PHA-E1 detector, penetrating MeV protons enhance the count-rates for E^* <50 keV and E^* >100 keV. For E^* >100, the spectrum becomes very flat. The plateau between the two enhancements is then the only resolvable feature which may contain contributions from MeV electrons.

After establishing the key signatures of penetrating MeV electrons and protons in the PHA spectra, we can assert which are the dominant species in the inner radiation belts at locations (C) and (D). In location (C) the count-rate of the E6 channel is comparable to the rates measured in the main electron belts at (A), (B) and (E). The same applies for the E6/P8 count-rate ratio. In location (D) the P8 count rate is very low, while E6 has almost a factor 20 stronger signal. If E6 gets strong contributions from MeV electrons, the characteristic signatures in the PHA spectra should be observable.

Instead, the MeV electron peak in the PHA-A spectra is not visible: count-rates increase above E^* ∼60 keV instead from 40 keV. The steep power-law drop-off at E^* >80 keV is also not present: the flatter spectrum is more consistent with the one at location (B), where MeV protons are present at high fluxes. In the PHA-E1 spectra, the contrast between the MeV proton enhancements at E^* <30 keV and E^* >80 keV and the plateau is much stronger than in location

(B), where electrons and protons co-exist. The shallow peak at E^* $\sim$110 keV attributed to MeV electrons is also not discernible. The spectrum for E^* $>$100 is flat, a signature of penetrating MeV protons.

The signatures in the spectra from the PHA-A and E1 detectors are therefore consistent with a dominant proton population in the radiation belt inward of Saturn's rings. Since the LEMMS response simulations indicate that the E-channels (including E6, plotted in Figure S.5) can measure $>$100 MeV protons, we assert that their signal is dominated by these species.

This analysis alone does not exclude the presence of MeV electrons, but rather that their characteristic signatures in the data are obscured by corresponding signatures of protons. The non-vanishing count-rates in the "plateau" feature in the PHA-E1 spectra (location C), may be due to MeV electrons, but that requires a detailed simulation of the spectra, in which case the magnetic field of the LET and the shielding of LEMMS by the Cassini spacecraft have to be added to the model shown in Figure S.2.

Relating instrument counts and intensities

Inversion process: In the simple case where the instrument measures particles in a narrow energy and narrow angular range, the conversion of count rates R (particles per time) into the differential intensity j (particles per energy range, solid angle, area, and time) is:

$$j = \frac{R}{G\,\Delta E} \tag{3}$$

where the geometry factor G is given from Equation 1 and ΔE is the effective energy range over which the instrument channel is considered sensitive. Most of the previous work with LEMMS was based on such a calibration.

For the environment studied in this paper, Equation 3 is not sufficient because of the presence of high energy protons that can penetrate the instrument housing and shielding. In such

cases, many LEMMS channels behave as integral channels and R is estimated by:

$$R\Big(\langle\alpha_{eq}\rangle, \lambda\Big) = \int_0^{\pi} \mathrm{d}\theta \int_0^{2\pi} \mathrm{d}\varphi \int_0^{\infty} \mathrm{d}E \; j(E, \alpha_{eq}) \; g_d(E, \theta, \varphi) \; \sin(\theta) \tag{4}$$

The differential geometry factor, g_d, was defined in Equation 2, which we derive from the simulations described above and use values illustrated in Figure S.3.

The particle kintetic energy is E and the equatorial pitch angle between the instrument boresight vector and the equatorial magnetic field ($\vec{B}_{eq}$), is α_{eq}. Any quantity in brackets, as $\langle\alpha_{eq}\rangle$, describes a direction along the instrument's boresight. The dependence of α_{eq} on θ and φ is given by combining Equations 5-7 that are described below. We also define λ as the effective latitude that in a dipole field would have the same ratio B_{eq}/B as in our magnetic field model. The latitude definition does not affect the final results.

The radiation belt intensity j is usually given as a function of α_{eq}. The relations between equatorial pitch angles α_{eq} and $\langle\alpha_{eq}\rangle$ and the local pitch angles α and $\langle\alpha\rangle$ (relative to the local magnetic field $\vec{B}$ at latitude λ of the spacecraft) derive from the conservation of the first adiabatic invariant and are:

$$\alpha_{eq}\Big(\alpha, \lambda\Big) = \arcsin\sqrt{\frac{B_{eq}}{B(\lambda)}\sin\alpha} \tag{5}$$

$$\langle\alpha\rangle\Big(\langle\alpha_{eq}\rangle, \lambda\Big) = \arcsin\sqrt{\frac{B(\lambda)}{B_{eq}}\sin\langle\alpha_{eq}\rangle} \tag{6}$$

The relation between the local pitch angle (measured relative to the magnetic field) and the angles θ and φ (measured relative to the instrument) depends on spacecraft location λ. This relation can be derived from the cosine law on a sphere, as for example given in Equation 4 of (*52*).

$$\alpha(\theta, \varphi, \langle\alpha\rangle) = \arccos[\cos\langle\alpha\rangle\ \cos\theta + \sin\langle\alpha\rangle\ \sin\theta\ \cos\varphi], \tag{7}$$

where $\langle\alpha\rangle$ is the local pitch angle into which the instrument boresight is pointing to. The two angles α (describing the particle) and $\langle\alpha\rangle$ (describing the instrument) are generally not the same but can be similar if the particle enters through the nominal opening of the telescope.

Before we quantitatively relate the radiation belt intensity j with the raw rate R, it is informative to point out that these two quantities can have a very different qualitative behavior, as we find in Saturn's innermost radiation belt (Fig. 2). Most notably R can show a dependence on latitude, even when filtering the data for $\langle\alpha_{eq}\rangle$ and L and accounting for reasonable systematic errors in these quantities. Such a latitudinal dependence is in stark contrast to the behavior of j, which is constant for all latitudes along the particle trajectory according to Liouville's theorem.

The latitude dependence of R results from the wide angular response of LEMMS's high energy channels, which for the channels considered here extends $\theta > 15^\circ$ away from the center of LEMMS's aperture, and the steep PAD in the inner radiation belts.

In order to better illustrate this, we consider an extremely wide angular response that can be described as omnidirectional. At any given latitude, the detector will receive fewer counts compared to the equator, because particles with certain α_{eq} mirroring at latitudes below the spacecraft, cannot contribute to the signal of the detector. Effectively, the α_{eq} range covered by the omnidirectional detector becomes smaller with increasing latitude and therefore the count rate of the detector decreases. This works similarly for any directional detector, like LEMMS, with a wide but finite angular resolution, even though the latitude dependence is not usually as pronounced as it is for omnidirectional detectors. An exception is when the pitch angle dependence of the intensity j is very steep, i.e. it evolves on angular scales much smaller than a channel's angular resolution.

In order to convert R into j we use a forward modeling approach. We select a narrow L-

shell range and bin the measured count rates of channels E7 and P8 in two dimensions. One dimension represents the look direction of the instrument. We quantify this with $\langle\alpha_{eq}\rangle$. The second dimension describes the location of the spacecraft relative to the magnetic equator. For this, we chose the equivalent latitude λ.

Then we assume an intensity distribution $j(E, \alpha_{eq})$ in the radiation belt at this L-shell and calculate $R(\langle\alpha_{eq}\rangle, \lambda)$ for all bins using Equation 4. The functional form of the intensity, j, assumed here is

$$j = A(E)\ J(\alpha_{eq}) \tag{8}$$

$$A(E) = \left(\frac{E}{E_0}\right)^{\gamma} \frac{j_A}{1 + \mathrm{e}^{(E-10^{Ec})/K_T}} \tag{9}$$

$$J(\alpha_{eq}) = \frac{1 + \mathrm{e}^{(C-\alpha_0)/k_t}}{\sin^N \alpha_0} \frac{\sin^N \alpha_{eq}}{1 + \mathrm{e}^{(C-\alpha_{eq})/k_t}} \tag{10}$$

with $E_0 = 39000$keV, $K_T = 0.05 \cdot 10^{Ec}$, $\alpha_0 = 90°$, and $k_t = 0.18°$.

The function $A(E)$ describes a power-law with exponent γ, with j_A the radiation belt intensity at $E = E_0$ and $\alpha = \alpha_0$. The power law cuts off at energy $10^{Ec} = 20$GeV. This value was selected since higher energy protons cannot be trapped around Saturn (*30*). The function $J(\alpha_{eq})$ describes a pitch angle distribution following a sine-function to the power of N. The distribution drops sharply into the loss cone inward of angle C. The loss cone angle is calculated for each location based on the chosen magnetic field model.

Based on the assumed intensity distribution (Equation 8) we numerically calculate reconstructed rates R_r for each bin (Equation 4) and compare with the measured rates R_m for each respective bin. The discrepancy between R_r and R_m is quantified via the root-mean-square (RMS) error $\Delta = \sqrt{\sum_i^I (\delta)^2}/I$ with $\delta = \log R_r^i - \log R_m^i$, where i runs over all I bins and channels. The free parameters are iterated until a good match between modeled and measured rates is found. The iteration is done using the CONSTRAINED_MIN function available in the

commercial software Interactive Data Language (IDL by Harris Geospatial Solutions, Inc.). After optimization, we find RMS errors of $\Delta < 0.1$, equivalent to the model rates being between $1/10^{\Delta} = 80\%$ and $10^{\Delta} = 130\%$ of the measured rate. The maximum error in a single bin is always $\delta < 1$.

We compare sample model and measured rates as a function of pitch angle and latitude in Figure S.6 (panels A-D). Panels E and F compare all binned, measured rates with the reconstructed count rates. The resulting differential intensities are plotted in Figures 3 and 4. It can be seen that the reconstruction reproduces all rates of any magnitude similarly well.

Upper flux limits: The method used to obtain the upper flux limits for non-proton species and for <25 MeV protons shown in Figure 3 is explained with the help of the data plotted in Figure S.7. The channel used in this example has a nominal response to 510-832 keV electrons (C7). All panels include data obtained between L=1.095 and L=1.105, where the intensity is highest.

The C7 measurements are well organized as a function of magnetic latitude (Figure S.7A) and shows an isotropic PAD (Figure S.7D), even in the loss cone, for every latitude. That is a typical behavior of a channel which is dominated by penetrating radiation from trapped particles. . In contrast, a channel with a high SNPR, like E7 that has been extensively used here, has a much more scattered count-rate distribution over latitude (Figure S.7C). This scatter at any selected, small latitude range is due to the superimposed pitch angle dependence of the signal.

The uncertainty for the strength of the residual signal outside the loss cone, after we subtract the penetrating radiation rate, is determined by the 1σ value of the count rates at the given L-shell. It is this value that we use in order to obtain the upper limits of Figure 5. In the case of channel C7, its rate varies between 1.4-2.0 Hz, depending on the latitude range chosen. A value

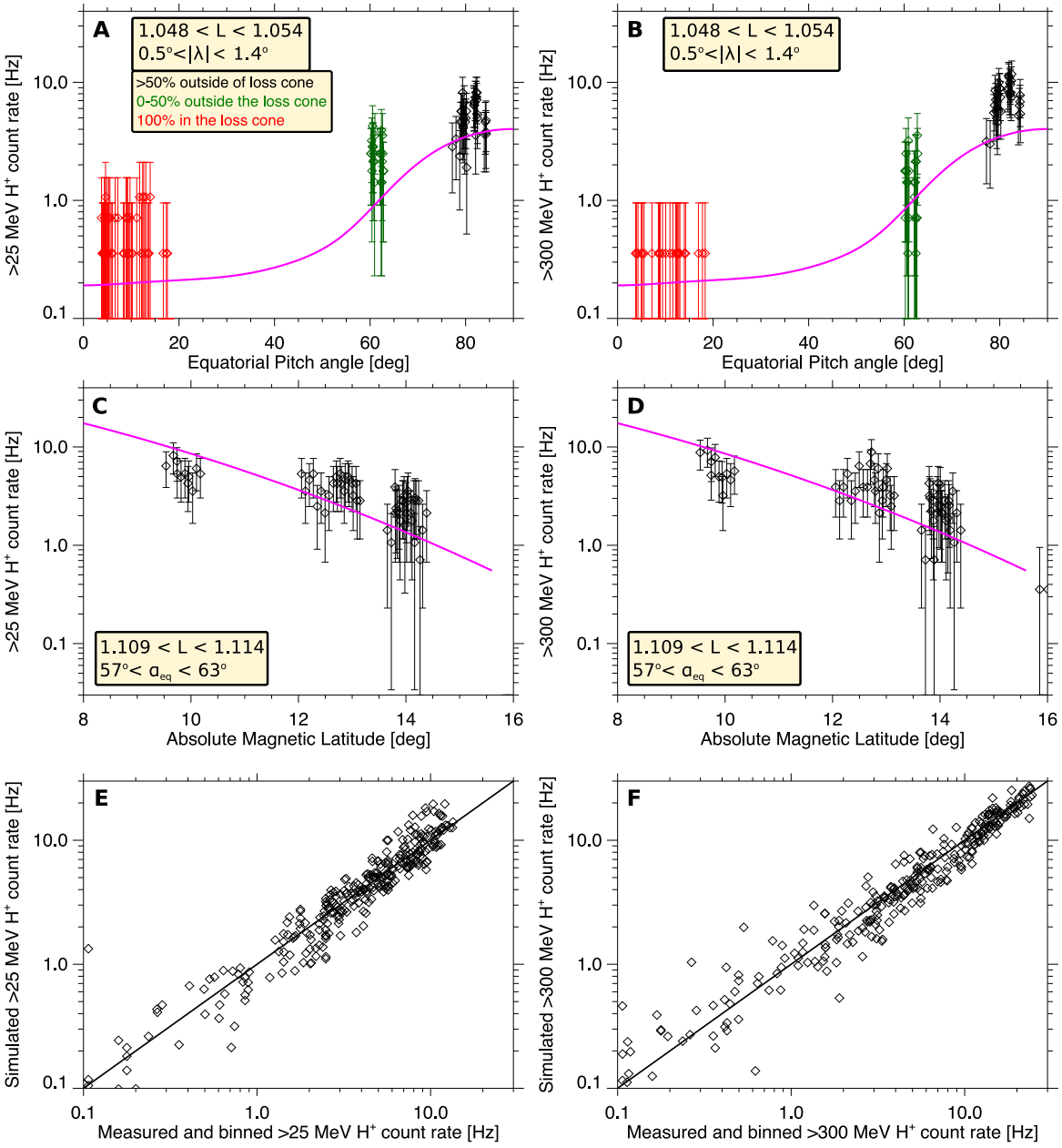

Figure S.6: Comparison of measured and reconstructed count rates. Left and right panels are for >25 MeV and >300 MeV protons, respectively. The model results are shown with a magenta curve in Panels A-D. Panels A and B show data selected from a narrow L-shell and magnetic latitude range, while data in C and D are from a narrow L-shell and α_{eq} range. In panels E and F we compare data from all L-shells (assembled in small L-shell, magnetic latitude and α_{eq} bins) with the simulated rates.

of 1.7 Hz was used for Figure 3. Conversion of this count-rate to an upper flux limit is done through Equation 3. These limits are accurate to about 30%. The same approach was used with all other LEMMS channels shown in Figure 3.

Limits for the electron fluxes in the MeV range could not be derived, but have to be small because even the respective LEMMS channels appear to be dominated by protons. Proton dominance is indicated by the E7 channel ($>$300 MeV protons and $>$7 MeV electrons) showing gross similarities in its L-shell profile with the P8 channel ($>$25 MeV protons, no electrons).

For CHEMS protons, we estimate a total sampling time of $\sim$384 minutes in the inner trapping region. The mass (M) to mass-per-charge (M/Q) event matrix revealed no accumulation of proton counts, so assigning a single count to protons as an upper limit is a reasonable guess. Since the energy stepping in CHEMS lasts 32 s, for each proton energy the sampling time was (384*60 s)/(32 s) = 720 s, which, using Equation 3, translates to a flux of 5.8 $cm^{-2}sr^{-1}s^{-1}MeV^{-1}$ for the 27-220 keV energy range where triple coincidence measurements are possible. This upper limit can be used for any ion species that CHEMS can resolve, not just protons.

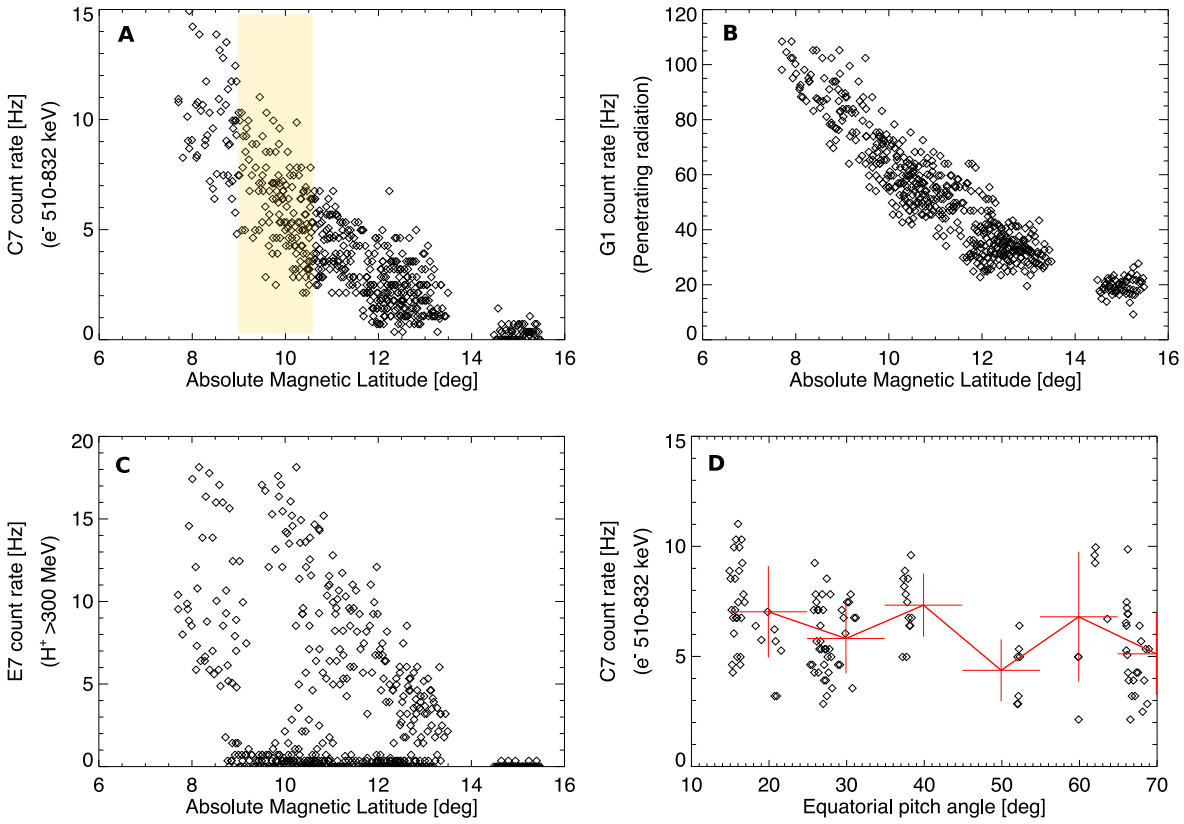

Figure S.7: Illustration on the derivation of the upper limit intensities shown in Figure 5: Panel (A): Magnetic latitude dependence of LEMMS C7 count rates (510-832 keV e^- nominally). Panel (B): Magnetic latitude dependence of LEMMS channel G1 rates, a channel that is designed to measure only penetrating radiation, Panel (C): Magnetic latitude dependence of LEMMS channel E7, without α_{eq} filtering, Panel (D): Dependence of C7 count rates over α_{eq}, for the latitude range marked with the shaded area in Panel A. Binned rates every 10° of α_{eq} are also shown in red.

References and Notes

48. S. Agostinelli, *et al.*, *Nuclear Instruments and Methods in Physics Research Section A: Accelerators, Spectrometers, Detectors and Associated Equipment* **506**, 250 (2003).

49. G. Santin, V. Ivanchenko, H. Evans, P. Nieminen, E. Daly, *Nuclear Science, IEEE Transactions on* **52**, 2294 (2005).

50. K. Yando, R. M. Millan, J. C. Green, D. S. Evans, *J. Geophys. Res. (Space Physics)* **116** (2011). A10231.

51. E. Roussos, *et al.*, *Icarus* **274**, 272 (2016).

52. W. Li, *et al.*, *Geophys. Res. Lett.* **40**, 4526 (2013).